Biochimie 94 (2012) 673–683

Contents lists available at SciVerse ScienceDirect

Biochimie

journal homepage: www.elsevier.com/locate/biochi

Research paper

Eukaryotic extracellular catalase–peroxidase from *Magnaporthe grisea* – Biophysical/chemical characterization of the first representative from a novel phytopathogenic KatG group

Marcel Zámocký [a,d,*], Enrica Droghetti [b], Marzia Bellei [c], Bernhard Gasselhuber [a], Martin Pabst [a], Paul G. Furtmüller [a], Gianantonio Battistuzzi [c], Giulietta Smulevich [b], Christian Obinger [a]

[a] Division of Biochemistry, Department of Chemistry, Vienna Institute of Biotechnology (VIBT) at BOKU – University of Natural Resources and Life Sciences, Muthgasse 18, A-1190 Vienna, Austria
[b] Department of Chemistry "Ugo Schiff", University of Florence, Sesto Fiorentino (FI), Italy
[c] Department of Chemistry, University of Modena and Reggio Emilia, Modena, Italy
[d] Institute of Molecular Biology, Slovak Academy of Sciences, Bratislava, Slovakia

ARTICLE INFO

Article history:
Received 18 July 2011
Accepted 21 September 2011
Available online 29 September 2011

Keywords:
Extracellular catalase–peroxidase
Peroxidases–catalase superfamily
Phytopathogen
Oxidative stress
Resonance Raman spectroscopy
Reduction potential

ABSTRACT

All phytopathogenic fungi have two catalase–peroxidase paralogues located either intracellularly (KatG1) or extracellularly (KatG2). Here, for the first time a secreted bifunctional, homodimeric catalase–peroxidase (KatG2 from the rice blast fungus *Magnaporthe grisea*) has been produced heterologously with almost 100% heme occupancy and comprehensively investigated by using a broad set of methods including UV–Vis, ECD and resonance Raman spectroscopy (RR), thin-layer spectroelectrochemistry, mass spectrometry, steady-state & presteady-state spectroscopy. RR spectroscopy reveals that MagKatG2 shows a unique mixed-spin state, non-planar heme *b*, and a proximal histidine with pronounced imidazolate character. At pH 7.0 and 25 °C, the standard reduction potential $E^{\circ\prime}$ of the Fe(III)/Fe(II) couple for the high-spin native protein was found to fall in the range typical for the KatG family. Binding of cyanide was relatively slow at pH 7.0 and 25 °C and with a K_d value significantly higher than for the intracellular counterpart. Demonstrated by mass spectrometry MagKatG2 has the typical Trp118-Tyr251-Met277 adduct that is essential for its predominantly catalase activity at the unique acidic pH optimum. In addition, MagKatG2 acts as a versatile peroxidase using both one- and two-electron donors. Based on these data, structure–function relationships of extracellular eukaryotic KatGs are discussed with respect to intracellular KatGs and possible role(s) in host–pathogen interaction.

1. Introduction

The peroxidase–catalase superfamily (named according to the two main enzymatic activities), also known as the non-animal superfamily or the superfamily of bacterial, fungal and plant heme peroxidases, is very likely the most abundant line of heme peroxidases in both prokaryotic and eukaryotic cells [1,2]. The first classification of this superfamily presented by K.G. Welinder in 1992 [3] was mainly based on structural homology and showed the presence of three main classes (Class I, II & III). Originally, Class I was defined to contain solely intracellular prokaryotic and eukaryotic non-glycosylated heme peroxidases (without disulfide

Abbreviations: 5c, five-coordinated; 6c, six-coordinated; APx, ascorbate peroxidase; ARP, *Arthromyces ramosus* peroxidase; BP1, barley peroxidase type 1; CAI, codon adaptation index; CAPS, 3-(cyclohexylamino)propane-1-sulfonic acid; CCD, charge-coupled device; CcP, cytochrome *c* peroxidase; CIP, *Coprinus cinereus* peroxidase; CT, charge transfer; L-DOPA, 3,4-dihydroxy-L-phenylalanine; $E^{\circ\prime}$, reduction potential, referred to the standard hydrogen electrode, measured at pH 7.0; ECD, electronic CD; ESI, electrospray ionization; HA, hydroxyapatite; HGT, horizontal gene transfer; HRP, horseradish peroxidase; HS, high-spin; KatG, catalase–peroxidase; IPTG, isopropyl-β-thiogalactopyranoside; KatG1, intracellular eukaryotic catalase–peroxidase; KatG2, extracellular eukaryotic catalase–peroxidase; LC, liquid chromatography; LiP, lignin peroxidase; LS, low-spin; MagKatG2, catalase–peroxidase from *Magnaporthe grisea*; MCAC, metal chelate affinity chromatography; MCD, monochlorodimedone; MOPS, 4-morpholinepropane sulfonic acid; MnP, manganese peroxidase; NJ, neighbor-joining method; OTTLE, optically transparent thin-layer electrochemistry; QS, quantum mixed-spin; RR, resonance Raman; RT-PCR, reverse-transcription PCR; SBP, soybean peroxidase; SHE, standard hydrogen electrode.

* Corresponding author. Metalloprotein Research Group, Division of Biochemistry, Department of Chemistry, Vienna Institute of Biotechnology at BOKU – University of Natural Resources and Life Sciences, Muthgasse 18, A-1190 Vienna, Austria. Tel.: +43 1 47654 6078; fax: +43 1 47654 6059.
E-mail address: marcel.zamocky@boku.ac.at (M. Zámocký).

0300-9084
doi:10.1016/j.biochi.2011.09.020

bridges and Ca^{2+}-binding) with (archae)bacterial bifunctional catalase–peroxidases, fungal cytochrome *c* peroxidases and plant ascorbate peroxidases comprising the three main clades [3]. Recent phylogenetic and genomic analyses revealed the presence of two additional clades of hybrid-type peroxidases and clearly demonstrated that Class I is the only class with representatives in all domains of life [2,4,5].

Additionally, these analyses have provided details on the eukaryotic distribution of bifunctional catalase–peroxidase (KatG) [1,2,6]. Phylogenetic reconstruction revealed that *katG* genes most probably originated in ancestral *Negibacteria* (proteobacterial predecessors) [2,5] and were acquired by ancient ascomycete fungi via horizontal gene transfer (HGT) from Bacteroidetes [2]. Fig. 1 demonstrates the presence of two distinct groups of fungal KatG [7] with intracellular enzymes (KatG1) present both in non-pathogenic and pathogenic fungi [7,8] and, most interestingly, extracellular representatives (KatG2) exclusively found in phytopathogenic fungi [2,7,9,10] where these oxidoreductases seem to play an important role in host–pathogen interaction. For example, KatG2 of the rice blast fungus *Magnaporthe grisea* has been shown to protect the pathogen from increased levels of hydrogen peroxide that accumulated in rice epidermal cells at the early stage of infection [9]. Secretion of KatG2 together with a typical (monofunctional) catalase is important for hyphal growth after host tissue penetration and for maintaining the integrity of fungal cell walls [10]. The distribution of secreted catalase–peroxidase exclusively in phytopathogens renders this group an interesting target for pest control. However, this needs a comprehensive understanding of its functional and structural features as well as characteristics. Recently, the recombinant form of the intracellular counterpart (KatG1 of *M. grisea*) has been investigated in detail [8]. Here, the first biophysical and biochemical investigation of an extracellular bifunctional catalase–peroxidase is presented. It includes the heterologous recombinant expression of KatG2 from *M. grisea*, MagKatG2 (in databases also named MgrCP02 or CPXB), in *Escherichia coli* and its structural and functional analysis. We report the (i) presence of KatG-typical posttranslational modifications, (ii) a comprehensive spectral (UV–Vis and resonance Raman) investigation of the ferric and ferrous form, (iii) the standard reduction potential of the Fe(III)/Fe(II) couple of the high-spin native protein as well as (iv) kinetic analyses of cyanide binding, hydrogen peroxide degradation and one-electron oxidation of electron donors of differing chemical structure (using peroxyacetic acid instead of H_2O_2). Data are compared with KatG1 from *M. grisea* as well as with prokaryotic KatGs that – in contrast to the eukaryotic enzymes – are well studied including elucidation of crystal structures and proposal(s) of reaction mechanism(s) [11,12].

2. Materials and methods

2.1. Organism and gene synthesis

Throughout this work *M. grisea* strain 70-15 was used as the reference strain with completely sequenced genome [13]. It was grown on MPG agar plates or MPG liquid medium as reported previously [8]. The gene coding for MagKatG2 is located on chromosome VI and contains 5 introns (see http://peroxibase.toulouse.inra.fr for details). In a first attempt to test its expression an internal portion of cDNA synthesized from mRNA of a paraquat-induced *M. grisea* culture was amplified using Cloned AMV First Strand cDNA Synthesis Kit (Invitrogen). For RT-PCR specific internal primers Mag2int1fwd and Mag2int1rev were used (Supplemental Table 1). Conditions of RT-PCR were as follows: 30 cycles of denaturation at 95 °C for 30 s, followed by 30 s annealing at 56 °C and 40 s elongation at 72 °C. Resulting PCR products were analyzed by agarose gel electrophoresis (1.2% agarose in TBE, Biozym) and

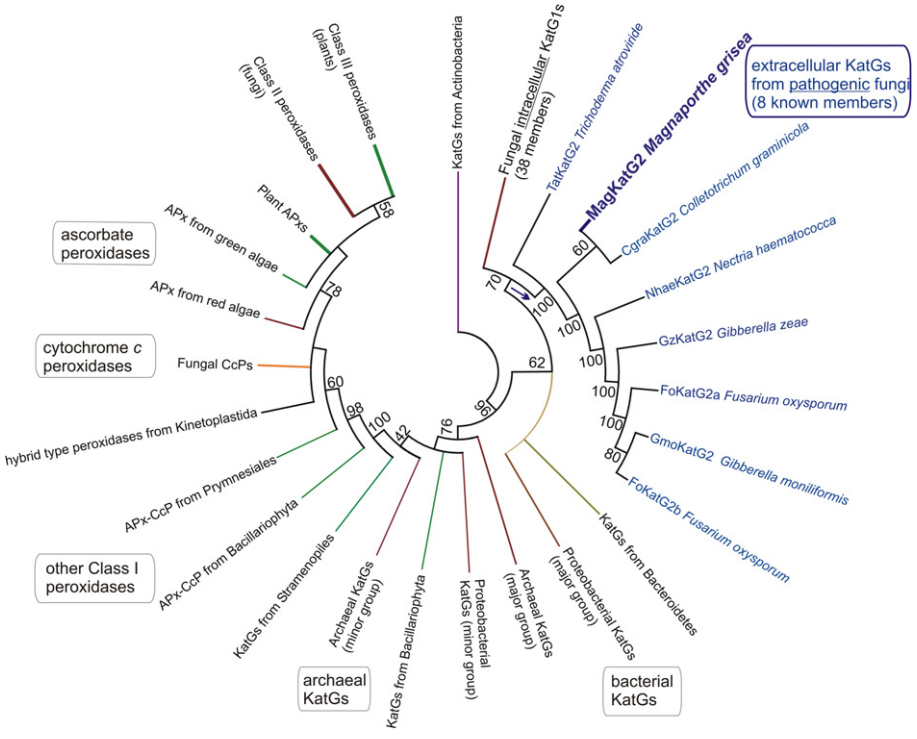

Fig. 1. Condensed circular evolutionary tree of Class I peroxidases with focus on catalase–peroxidases. The evolution of fungal enzymes from KatGs from Bacteroidetes is evident as is the branching of extracellular enzymes (KatG2, highlighted in blue) from intracellular (KatG1) counterparts (blue arrow). Most interestingly, all so far identified secretory KatGs are found in pathogenic organisms (May, 2011). Phylogenetic relationships were reconstructed using the NJ method of the MEGA 5 package (http://megasoftware.net/). Abbreviations of species correspond with their names in PeroxiBase (http://peroxibase.toulouse.inra.fr). Numbers in the nodes represent bootstrap values for 1000 replications. (For interpretation of the references to color in this figure legend, the reader is referred to the web version of this article.)

compared with DNA molecular weight standards (Fermentas). Obtained cDNA fragments were sequenced at LGC Genomics. A KatG2-typical signal sequence of 69 bp was found at the start of the coding region [7]. However, because of problems in heterologous expression (details not shown), we decided to clone the entire coding region of *MagkatG2* without the signal sequence in the bacterial vector pET21a (Novagen) for intracellular expression. For this purpose, the intronless gene was synthesized (GenScript) with codon optimisation for *E. coli* expression. The codon adaptation index (CAI) was improved from 0.66 (natural sequence) to 0.98 (synthetic gene) (Supplemental Fig. 1). The translation product of the synthetic gene revealed the same amino acid sequence as native MagKatG2 and included a C-terminal hexa-histidine tag (GenBank accession JF937064).

2.2. Heterologous expression and purification of recombinant MagKatG2

Recombinant MagKatG2 was expressed in *E. coli* strain BL21 DE3 Star (Invitrogen) in M9ZB medium upon induction by 0.5% ($^{w}/_{v}$) lactose. Cell pellets of 15 h old cultures grown at 16 °C were resuspended and homogenized under conditions as described for MagKatG1 [8]. After centrifugation (20 min at 20000 g) the crude homogenate was applied onto a Chelating Sepharose Fast Flow column (30 mL, GE Healthcare) loaded with Ni^{2+} ions. Unbound protein was removed by washing with 150 mL of buffer A (50 mM sodium phosphate, pH 8.0, 500 mM NaCl and protease inhibitors PMSF and Leupeptin). Bound protein was eluted with a linear gradient of buffer A to 100% buffer B (50 mM sodium phosphate, pH 7.5, 500 mM NaCl and 500 mM imidazole). Furthermore, collected heme protein with His_6-tag (MagKatG2) was purified using a hydroxyapatite column (25 mL, Sigma Chemicals) as previously described [14]. After washing with 75 mL of 5 mM phosphate buffer, pH 7.5, fractions containing high-spin MagKatG2 were eluted with 50 mM phosphate buffer, pH 7.7. Low-spin fractions could only be eluted with 200 mM phosphate buffer, pH 8.0, and were not used for further work. High-spin fractions were pooled, concentrated with Centriprep 50 K (Millipore) (30 min at 1500 g) and loaded onto a Superdex 200 column (250 mL, GE Healthcare) for final purification as described for MagKatG1 [8].

For protein electrophoresis NuPAGE Novex Bis-Tris gradient gels (4–12%) with 15 wells (Invitrogen) were used (running buffer: MOPS-SDS). Gels were stained with Coomassie Brilliant Blue (Sigma Aldrich) or immunoblotted onto a nitrocellulose membrane (Amersham Biosciences) for detection of MagKatG2 by using a homemade polyclonal antibody raised against catalase–peroxidase from the cyanobacterium *Synechocystis* PCC 6803.

2.3. MS analysis

Tryptic peptides of purified MagKatG2 were injected to a capillary LC-ESI-MS system consisting of a BioBasic C18 analytical column (150 mm, 60.18 mm, 5 mm, Thermo Scientific), a Dionex Ultimate 3000 capLC and a Waters Q-TOF Ultima with standard ESI-source. Solvent A was 65 mM ammonium formate, pH 3.0, and solvent B was 100% acetonitrile. Positive ions in the range from m/z 50 to 1800 were measured. Capillary voltage was 3.2 kV and cone voltage 35 V, source temperature was 100 °C and desolvation temperature 120 °C. Data were evaluated using MassLynx 4.0 software and herein the MaxEnt3 deconvolution and deisotoping feature.

2.4. UV–Vis and electronic circular dichroism

UV–visible spectra of MagKatG2 were routinely recorded with a Hitachi U-3900 or a double-beam Cary 5 (Varian, Palo Alto, CA, US) spectrophotometer in the range 800–200 nm at 25 °C. The molar absorption coefficient of the ferric, high-spin form at Soret band maximum (102 600 M^{-1} cm^{-1}) was determined from the slope of the linear plot of absorbance at 404 nm *versus* protein concentration determined by the Bradford method. Heme occupancy was determined with the pyridine–hemochrome method [15]. The absorption coefficient of pure MagKatG2 at 280 nm was calculated to be ε_{280nm} = 147 800 M^{-1} cm^{-1} using the protein sequence (Expasy server).

Low-spin cyanide complexes were formed upon mixing of 5.5 μM of purified protein with increasing concentrations of sodium cyanide in 5 mM phosphate buffer, pH 7.5. Apparent bimolecular rate constant of complex formation was determined by conventional stopped-flow spectroscopy (SX-18MV from Applied Photophysics) as described previously [8]. Ferrous MagKatG2 was produced by the addition of freshly prepared anaerobic solution of 2 mM sodium dithionite.

Electronic circular dichroism (ECD) spectra were recorded on Chirascan equipped with a thermostatically controlled cell holder (Applied Photophysics, Leatherhead, U.K.). For recording far-UV spectra (260–190 nm), the quartz cuvette had a pathlength of 1 mm. The spectral bandwidth was 5 nm, step size 1 nm, and the scan time was 120 s (scan period 25 μs × 20,000 counts). Deconvolution of ECD spectra was performed with DichroWeb software at http://dichroweb.cryst.bbk.ac.uk based on the SP175 database [16,17]. For comparison, secondary structure elements were predicted with PSIPRED server [18] and a homology model of MagKatG2 was constructed using the SWISS-MODEL workspace [19].

2.5. Resonance Raman spectroscopy

Resonance Raman (RR) spectra of the ferric forms of MagKatG2 were obtained by excitation with the 406.7 nm line of a Kr^{+} laser (Coherent, Innova 302). RR spectra of the ferrous forms were obtained by excitation with the 441.6 nm line of a He–Cd laser (Kimmon IK4121R-G), and the 457.9 nm and 476.5 nm lines of an Ar^{+} laser (Innova 90/5, Coherent). The backscattered light from a slowly rotating 5 mm NMR tube was collected and focused into a computer-controlled triple spectrometer (consisting of two Acton Research SpectraPro 2300i and a SpectraPro 2500i in the final stage with a 1800 or alternatively a 3600 grooves/mm grating) working in the subtractive mode, equipped with a liquid nitrogen-cooled CCD detector (Roper Scientific Princeton Instruments). All RR measurements were repeated several times under the same conditions to ensure reproducibility. Electronic absorption spectra in a 5 mm NMR tube were collected before and after the RR spectra.

Polarized spectra were obtained by inserting a Polaroid analyzer between the sample and the entrance slit of the monochromator. The depolarization ratios of the bands at 314 and 460 cm^{-1} of CCl_4 were measured to check the reliability of the polarization measurements. The values obtained, 0.73 and 0.00, compare well with the theoretical values of 0.75 and 0.00, respectively.

To improve the signal-to-noise ratio, a number of spectra were accumulated and summed only if no spectral differences were noted. RR spectra were calibrated with carbon tetrachloride, n-pentane, indene, dimethyl sulfoxide as standards to an accuracy of 1 cm^{-1} for intense isolated bands. Prior to the spectra analysis contributions from the featureless background was subtracted. Peak intensities and positions have been evaluated using a curve-fitting program (Lab Calc, Galactic), with a Lorentzian line shape. The frequencies of the bands were optimized with an accuracy of 1 cm^{-1}, and the bandwidths with an accuracy of 0.5 cm^{-1}.

The ferric form of the protein was obtained by diluting an aliquot of a stock protein solution into an appropriate buffer. The following buffers were used: 100 mM MES buffer, pH 5.7; 100 mM

phosphate buffer, 7.5; 100 mM CAPS buffer, pH 10.5–11.0. The ferrous form was obtained by adding a small volume (2–5 μL) of a fresh sodium dithionite solution (10–20 g/L $Na_2S_2O_4 \cdot 2H_2O$) to 40 μL of a deoxygenated protein solution. Sample concentration was about 20–30 μM for electronic absorption spectra and about 30–80 μM for RR experiments.

2.6. Spectroelectrochemistry

Determination of the $E^{\circ\prime}$ of the Fe(III)/Fe(II) couple of highly purified MagKatG2 was carried out using a homemade OTTLE (optically transparent thin-layer spectro-electrochemical) cell [20]. The three-electrode configuration consisted of a gold mini-grid working electrode (Buckbee-Mears), a homemade $Ag/AgCl/KCl_{satd}$ microreference electrode, separated from the working solution by a Vycor set, and a platinum wire as counter-electrode [21]. The reference electrode was calibrated against a saturated calomel (HgCl) electrode before each set of measurements. All potentials are referenced to the standard hydrogen electrode.

Potentials were applied across the OTTLE cell with an Amel model 2053 potentiostat/galvanostat. A constant temperature was maintained by a circulating water bath, and the OTTLE cell temperature was monitored with a Cu-costan microthermocouple. UV–visible spectra were recorded using a Varian Cary C50 spectrophotometer. Spectra of 18 μM MagKatG2 in 50 mM sodium phosphate buffer, pH 7.0, containing 10 mM NaCl, were recorded at various applied potentials (25 °C). Paraquat (500 μM), lumiflavine-3-acetate, methylene blue, phenazine methosulfate and indigo disulfonate (2 μM each) were used as redox mediators.

2.7. Overall kinetic parameters

Catalase activity was determined both polarographically and spectrophotometrically. Polarographic analysis used a Clark-type electrode (Hansatech) inserted into a stirred water bath. The photometric determination was based on the measurement of the degradation of H_2O_2 at 240 nm (ε = 39.4 M^{-1} cm^{-1}) [22]. For spectrophotometric measurements, one unit was defined as the amount of enzyme catalysing the conversion of 1 μmol of H_2O_2 per min at an initial concentration of 15 mM H_2O_2 at pH optimum and 25 °C.

Peroxidatic activity was monitored spectrophotometrically by using 1 mM peroxyacetic acid and various one-electron donors (1 mM): 5-amino salicylic acid, guaiacol, L-DOPA, o-dianisidine, catechol, pyrogallol, resorcinol, tetramethylbenzidine and ascorbate (all from Sigma–Aldrich). One unit of peroxidase was defined as the amount of enzyme that oxidizes 1 μmol of selected electron donor per min at pH optimum and 25 °C. Potential chlorination and bromination activity was followed by halogenation of 100 μM monochlorodimedone dissolved in 100 mM phosphate buffer, pH 7.0, containing 10 mM H_2O_2 and either 10 mM sodium bromide or 100 mM sodium chloride. Rates of halogenation were determined from the initial linear part of the time traces using an absorption coefficient for monochlorodimedone at 290 nm of 19.9 mM^{-1} cm^{-1} [23].

3. Results

3.1. MagkatG2 gene and its heterologous expression

In contrast with the gene coding for MagKatG1 [8] and with other mostly intronless ascomycete *katG* genes in general, *MagkatG2* contains 5 introns (http://peroxibase.toulouse.inra.fr) interrupting the 2361 bp long coding sequence. First expression of *MagkatG2* was followed in the rice blast fungus grown in liquid MPG medium for 4 days at 25 °C. Previous studies demonstrated that oxidative stress induces expression in various growth phases [24] with paraquat added to MPG up to 10 μM revealing highest induction. Mycelia were collected from these cultures by filtration and mRNA was isolated. Corresponding cDNA was prepared with the first strand cDNA synthesis kit. A short RT-PCR fragment located on exons V and VI was obtained with internal primers (Supplemental Table 1; EST database accession HS587019.1). Native expression of *MagkatG2* gene was further evidenced with nine additional cDNA fragments entered in EST database from various cDNA libraries of *M. grisea* (synonym, *Magnaporthe oryzae*, anamorph, *Pyricularia grisea*). Most of them originated from libraries obtained during the infection of rice leaves with rice blast fungus [25]. They were located in conidia, mycelia, appresorium and penetration peg (EST: CK916856) but also in perithecia of mated culture (CD034008). However, in all (ten) analyzed EST entries only the middle and 3′ terminal part of *katG2*-specific mRNA could be detected. The absence of 5′ terminal part could be explained with a possibly increased mRNA decay in 5′→3′ direction [26]. Since recently native expression of *MagkatG2* (CPXB) at protein level has been demonstrated [9], we decided to synthesize the whole coding region without its signal sequence for large scale intracellular *E. coli* expression (Supplemental Fig. 1).

Heterologous expression of *MagkatG2* was performed as already described for both bacterial and fungal catalase–peroxidase expression [14,27]. The only modification was the replacement of the inducer IPTG with 0.5% lactose that allowed higher cell densities of *E. coli* BL21 DE3 Star cultures and in consequence higher yields. On average about 25 mg of soluble MagKatG2 could be obtained by lysis from cell pellets of 1 L M9ZB medium. Progress in purification steps is summarized in Supplemental Table 2 and reflected by SDS-PAGE gels and Western blots shown in Fig. 2. Pure ferric high-spin protein had its Soret maximum at 404 nm, a Reinheitszahl (purity number, A_{404nm}/A_{280nm}) of 0.67–0.69 and a monomer size of 85 kDa (theoretical molar mass of monomer with one heme *b* and a His_6-tag is 85.30 kDa). Superdex 200

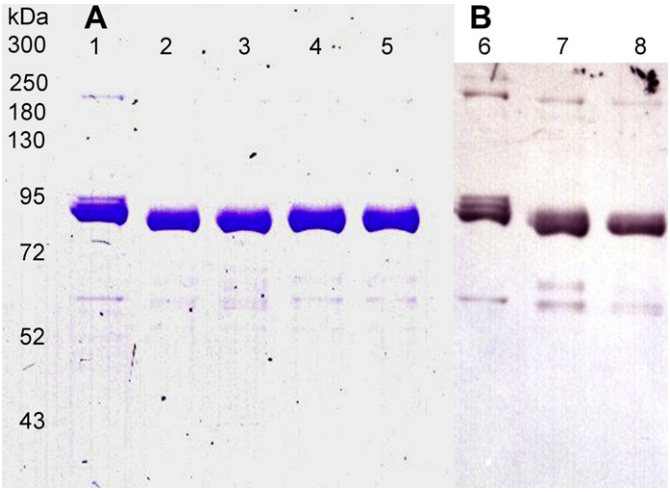

Fig. 2. SDS-electrophoresis of recombinant MagKatG2 under reducing conditions (A) and Western blot (B). (A) Coomassie Brilliant Blue-stained SDS-PAGE: lane 1, pooled Ni-MCAC gradient fractions (20–40% of the gradient); lane 2, pooled fractions after hydroxyapatite chromatography eluted with 50 mM phosphate buffer, pH 7.7; lane 3, pooled HA fractions eluted with 200 mM phosphate buffer, pH 8.0; lane 4, sample from lane 2 after Superdex 200 fraction 9; lane 5, same as lane 4, fraction 10. (B) Immunoblotting using a polyclonal antibody raised against cyanobacterial KatG from *Synechocystis* PCC 6803: lane 6, pooled Ni-MCAC gradient fractions; lane 7, hydroxyapatite fractions eluted with 50 mM phosphate buffer, pH 7.7; lane 8, hydroxyapatite fractions eluted with 200 mM phosphate buffer, pH 8.0.

chromatography clearly demonstrated the homodimeric nature of MagKatG2 (not shown) which was even evident in SDS-PAGE and Western blot analysis (Fig. 2).

For further identification of MagKatG2 SDS bands at 85 kDa and 180 kDa (Fig. 3) were subjected to peptide mapping using LC–ESI-MS. Recorded masses were analyzed with MS/MS ions search option of the Mascot software suite (http://www.matrixscience.com) and resulted in a sequence coverage of 95% (monomer) (Fig. 3A) and 62% (dimer, not shown). Additionally, MS analysis clearly demonstrated the presence of a covalent adduct between distal Trp118-Tyr251-Met277 that so far has only been demonstrated in prokaryotic and archaeal KatGs and is essential for the catalase activity of these bifunctional peroxidases [28–30]. Peptides containing the three amino acids (Fig. 3A) could be shown to be covalently linked via the Trp-Tyr-Met adduct and two of these (tri)peptides (Fig. 3C) were unequivocally identified in the mass spectrum and further MSMS analysis (Supplemental Fig. 2).

3.2. Spectroscopic and electrochemical investigations

Recombinant catalase–peroxidase is stable in the pH range 5.5 to pH 11.0 giving rise to almost identical UV–Vis spectra (data not shown). In addition, no aggregation or degradation or spectral changes of the ferric protein were observed during the time scale of spectroscopic measurements including RR spectroscopy (see below). Below pH 5.5 the protein unfolds and free heme, characterized by a Soret band at about 370 nm, is observed (data not shown). The ferric form exhibits all bands typical for a heme *b* containing peroxidase in the high-spin state, namely a Soret band with a maximum at 404 nm and a shoulder at 380 nm, Q-bands at 505 and 539 nm and a CT1 band at 640 nm (Fig. 4A). This latter band is broad and asymmetric and the second derivative spectrum (data not shown) reveals the presence of two bands at 640 nm and 654 nm. No bands characteristic of a low-spin (LS) heme are observed. We notice that the Soret band maximum is blue-shifted, not only with respect to the intracellular fungal counterpart MagKatG1 [8] but also to bacterial KatGs, by 2–5 nm [11].

The RR spectrum of ferric MagKatG2 (Fig. 4B,C and Supplemental Fig. 3) shows the presence of two sets of core size marker bands corresponding to two different species. One species with ν_3 at 1494 cm^{-1}, ν_{11} at 1553 cm^{-1}, ν_2 at 1569 cm^{-1} and ν_{10} at 1632 cm^{-1} is typical of a penta-coordinated high-spin (5cHS) heme form [31]. Based on the spectra in polarized light (data not shown) the intense band at 1624 cm^{-1} is assigned to the overlapping contribution of the 2- and 4-vinyl ν(C=C) stretching modes [32]. Furthermore, since the electronic absorption spectrum does not give any evidence of hexa-coordinated low-spin (6cLS) heme, the intense bands at 1503 cm^{-1} (ν_3), 1577 cm^{-1} (ν_2), and 1639 cm^{-1} (ν_{10}), (whose frequencies are typical of 6cLS hemes), are assigned to a penta-coordinated quantum mechanically mixed-spin (5cQS) state. Moreover, the intense band at 1524 cm^{-1} (ν_{38} of a 6cHS or 6cQS) suggest the presence of a 6c heme whose core size marker bands are hidden by the 5c species.

In the low-frequency region, the RR spectrum is extremely rich (Fig. 4C). Comparing the RR spectrum of MagKatG2 with that of SynKatG [33], horseradish peroxidase, isoenzyme C (HRP) [34], myoglobin [35], and cytochrome *c* [36] we tentatively assigned the bands at 286, 332, 442, 490/502, and 548 cm^{-1} to the γ_7, γ_6, γ_{22}, γ_{12}, and γ_{21} out-of-plane modes, respectively. Therefore, a remarkable enhancement and activation of several non-planar modes deriving from heme symmetry lowering induced by heme distortion is suggested.

Fig. 5A shows the UV–Vis spectra of ferrous MagKatG2 at pH 5.7, 7.5, and 11.0. At pH 7.5 both 5cHS and 6cLS heme states are present. In addition, the presence of a shoulder at about 404 nm clearly indicates that the protein is not fully reduced (see Fig. 5, panel A). A pH-induced transition is observed. At pH 5.7 the Soret maximum at 439 nm and the Q-bands at 587 and 555 nm are characteristic of a 5cHS heme, which coexists with a 6cLS species (Soret maximum at 424 nm). The latter form increases upon increasing the pH, and becomes dominant at alkaline pH (bands at 418, 525 and 555 nm). The RR spectra in the high frequency region are characteristic of a 5cHS (ν_3 at 1472 cm^{-1}) and a mixture of a 6cLS ferric and ferrous forms (ν_3 at 1500 cm^{-1}) heme, with the latter increasing upon increasing the pH (data not shown). At pH 7.5 (Fig. 5B) the spectrum is mainly characterized by a 5cHS heme (1472 cm^{-1}, ν_3; 1521 cm^{-1}, ν_{38}; 1555 cm^{-1}, ν_{11}; 1567 cm^{-1}, ν_2; 1588 cm^{-1}, ν_{37}; 1605 cm^{-1}, ν_{10}).

The RR low-frequency spectrum of ferrous MagKatG2 at pH 7.5 obtained with 441.6 nm excitation is characterized in the region of the Fe–Im stretching mode by an intense band at 241 cm^{-1}, with a shoulder at 251 cm^{-1}, and a band at 190 cm^{-1} (Fig. 5C). In order to identify the ν(Fe–Im) stretching mode, RR spectra of the ferrous forms were measured with different excitation wavelengths since the mode is strongly enhanced in resonance with the Soret band (at 439 nm) [37]. Upon excitation with the 457.9 and 476.5 nm lines the band at 241 cm^{-1} progressively disappears, while the bands at 251 and 190 cm^{-1} are almost unchanged. Therefore, the band at 241 cm^{-1} is assigned to a ν(Fe–Im) stretching mode. Since the protein cannot be completely reduced, upon 413.1 nm excitation the RR spectrum is characterized by bands due to both the ferric and the ferrous forms (data not shown).

In addition, the standard reduction potentials, $E^{\circ\prime}$, of the Fe(III)/Fe(II) couple in the high-spin native MagKatG2 has been determined at pH 7.0 and 25 °C by UV–vis spectroelectrochemistry and the electronic spectra measured at different applied potentials in the OTTLE cell are shown in Fig. 6. The $E^{\circ\prime}$ [Fe(III)/Fe(II)] value was determined from the corresponding Nernst plot (inset to Fig. 6) and was found to be (-210 ± 10) mV.

A 3D-model based on the closest bacterial phylogenetic neighbor, namely KatG from *Burkholderia pseudomallei* (PDB code 1mwv) [38] is presented in Supplemental Fig. 4. Additional, it depicts the ECD spectrum of MagKatG2 in its ferric and ferrous form suggesting a mainly α-helical structure that is not sensitive to the oxidation state of the enzyme. The calculated secondary structure content (Supplemental Table 3 and Supplemental Fig. 5) underlines the predominantly α-helical and low β-strand content typical for catalase–peroxidases and Class I peroxidases in general.

Cyanide converts the HS ($S = 5/2$) iron state to the LS ($S = 1/2$) state, thereby shifting the Soret peak of the Fe(III) form from 404 nm to 420 nm. Access and binding of cyanide to the active site was analyzed by conventional stopped-flow spectroscopy. Under conditions of excess cyanide, pseudo-first-order rate constants, k_{obs}, could be obtained from single-exponential fits of the rapid and dominating phase of the biphasic time traces (Fig. 7A). The slow (minor) phase was independent of the cyanide concentration. The apparent second-order rate constant (k_{on}) calculated from the slope of the linear plot of k_{obs} *versus* cyanide concentration (Fig. 7B) was $(5.4 \pm 0.2) \times 10^5$ M^{-1} s^{-1} at pH 7.0 and 25 °C. Since the value of the intercept was in the same order of magnitude as its standard deviation, k_{off} (and in consequence the dissociation constant, K_d) could not directly be obtained from the kinetic data. However, from thermodynamic binding studies, presented as spectral overlay for stepwise titration with increasing cyanide concentration (Fig. 7C), K_d was calculated to be (15.4 ± 1.1) μM (Fig. 7D).

3.3. Basic kinetic properties

The specific catalase and peroxidase activity as well as the pH-dependence of the bifunctional activity of highly purified

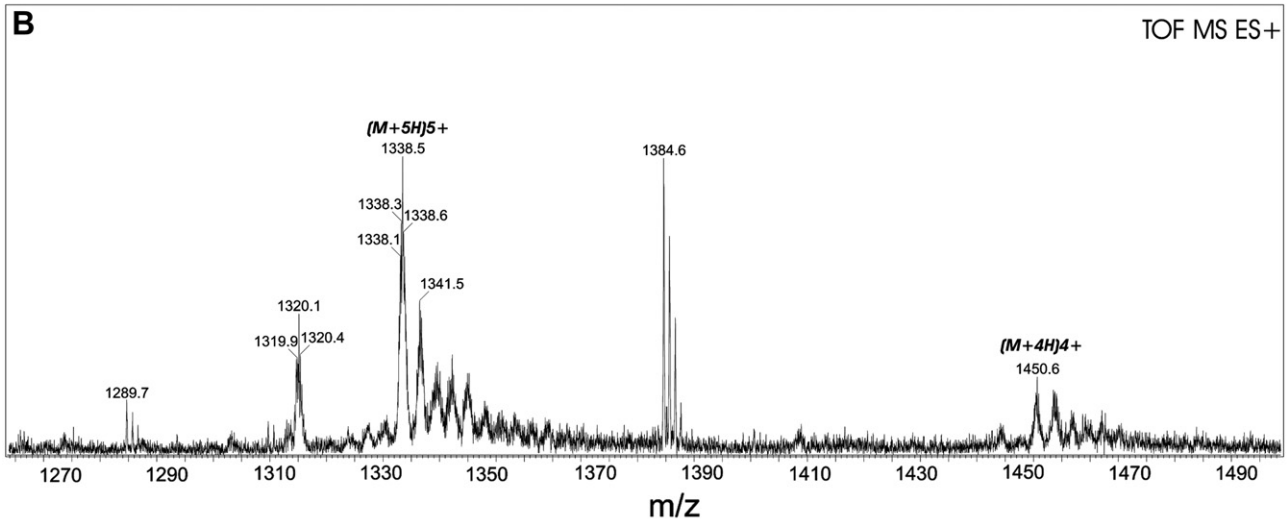

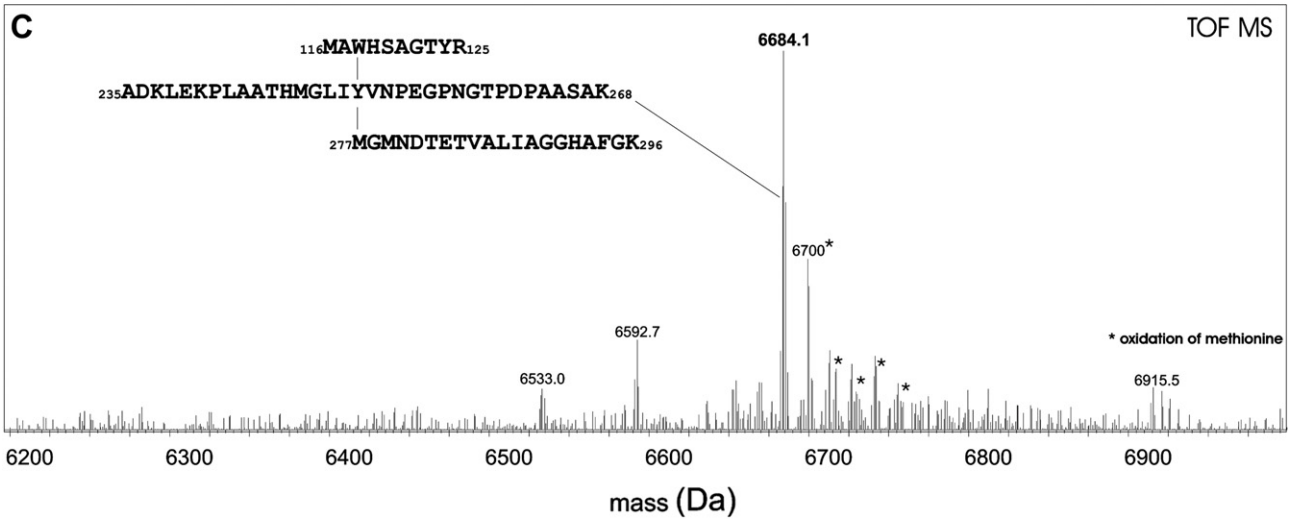

Fig. 3. (A) Analysis of tryptic digest of MagKatG2 monomeric band (~85 kDa) from SDS-PAGE (lane 5 in Fig. 2), by RP-ESI-MS. Sequence coverage was 95% (identified amino acids in red), peptides containing distal Trp118, Tyr251 and Met277 involved in KatG-typical adduct formation are highlighted in green. (B, C) Summarized mass spectrum. Covalently linked tri-peptide was found 4- and 5-times protonated (B). (C) Deconvoluted mass spectrum (M_i = 6684 Da, methionine residues not oxidized). (For interpretation of the references to color in this figure legend, the reader is referred to the web version of this article.)

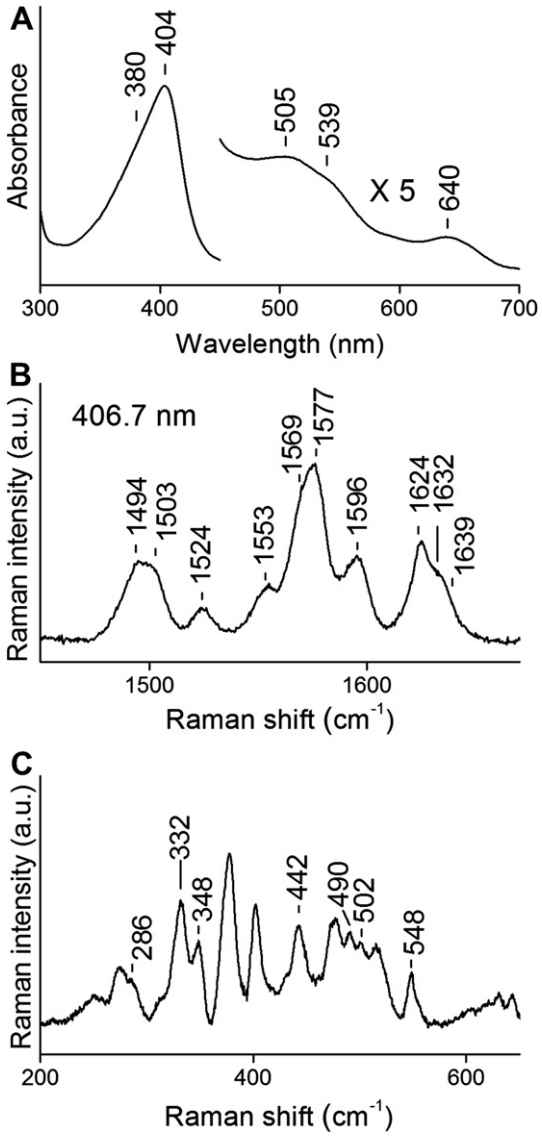

Fig. 4. UV–Vis (A) and RR spectra in the high (B) and low (C) frequency region of ferric MagKatG2 at pH 7.5. (A) The 450–700 nm region has been expanded by a factor of five. (B, C) RR spectra obtained with 406.7 nm excitation wavelength, 1 cm^{-1} resolution. (B) 5 mW laser power at the sample and 120 min total accumulation time. (C) 10 mW laser power at the sample and 150 min total accumulation time.

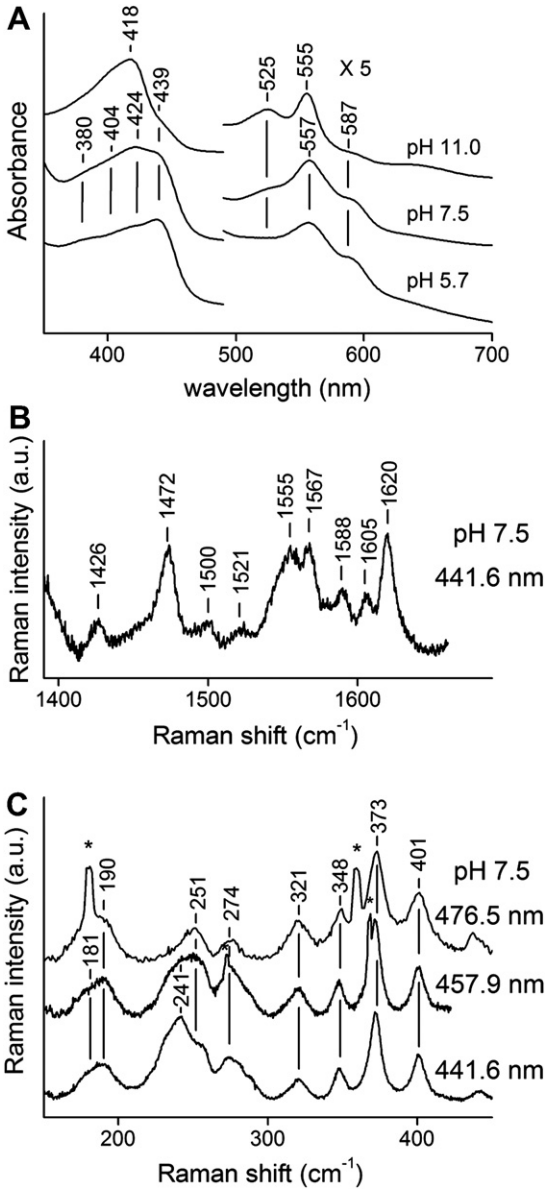

Fig. 5. (A) Electronic absorption spectra of ferrous MagKatG2 at various pH values. The region between 490 and 700 nm has been expanded 5-fold. The spectra have been shifted along the ordinate axis to allow better visualization. (B, C) RR spectra of ferrous MagKatG2 (pH 7.5). (B) High frequency region spectra obtained with 441.6 nm excitation wavelength, 1 cm^{-1} resolution, 15 mW laser power at the sample and 30 min total accumulation time. (C) Low-frequency region spectra obtained with different excitation wavelengths. The relative intensities of the bands are normalised to that of the ν_8 band (at 348 cm^{-1}). The asterisk '*', indicates plasma lines. Experimental conditions: 1 cm^{-1} resolution, 15 mW laser power at the sample and 120 min total accumulation time (441.6 nm excitation wavelength); 1 cm^{-1} resolution, 30 mW laser power at the sample and 120 min total accumulation time (457.9 nm excitation wavelength); 3 cm^{-1} resolution, 50 mW laser power at the sample and 60 min total accumulation time (476.5 nm excitation wavelength). Spectra have been shifted along the ordinate axis to allow better visualization.

MagKatG2 were investigated in detail. The pH optimum for the peroxidatic activity depended on the nature of one-electron donor (Table 1), whereas the optimum pH for hydrogen peroxide dismutation was 5.25 (Fig. 8) revealing some differences with intracellular fungal and bacterial KatGs. The K_m, k_{cat} and k_{cat}/K_m values for catalase activity at pH optimum were determined to be 3.84 mM (2.77 mM at pH 7.0), 6450 s^{-1} (3290 s^{-1}) and 1.68 $\times$ 10^6 M^{-1} s^{-1} (1.19 $\times$ 10^6 M^{-1} s^{-1}), respectively.

Since the natural peroxidase substrate of bacterial and fungal KatGs is unknown, various electron donors of different size and redox potential were probed at their respective pH optima (Table 1). The determined hierarchy regarding reactivity was resorcinol > o-dianisidine > L-DOPA > 5-amino salicylic acid > ascorbate > pyrogallol >> guaiacol > catechol. Tetramethylbenzidine as well as NADH could not be oxidized by KatG2, which, interestingly, featured a reasonable halogenation activity (Table 1).

4. Discussion

This work focused on a novel group of eukaryotic catalase–peroxidases that contain signal sequences for secretion [2,7] and without exception are found in phytopathogenic fungi. Recently, the physiological role of KatG2 secreted by *Magnaporthe oryzae* has been analyzed and shown to be important in H_2O_2 detoxification in order to cope with the host oxidative burst [9]. We have

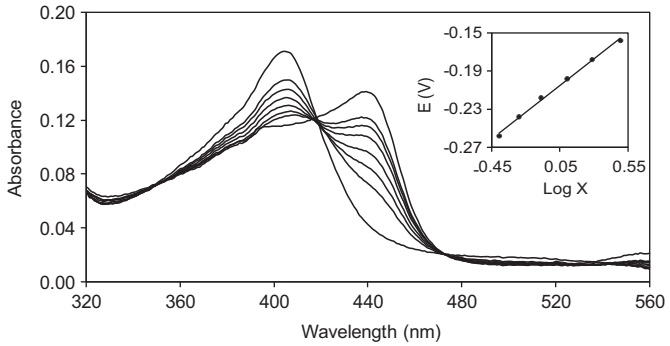

Fig. 6. Electronic spectra of high-spin MagKatG2 obtained at various potentials. Spectra were recorded at 25 °C. The inset depicts the corresponding Nernst plot, where X represents $[(A^{max}_{\lambda_{red}} - A_{\lambda_{red}})/(A^{max}_{\lambda_{ox}} - A_{\lambda_{ox}})]$, $\lambda_{ox} = 404$ nm and $\lambda_{red} = 439$ nm.

successfully produced the recombinant homodimeric form of *M. grisea* catalase–peroxidase 2 (MagKatG2) in high yield (comparable with the production of bacterial KatGs) thus allowing (i) the first characterization of this unique clade of extracellular bifunctional peroxidases and (ii) comparison with its intracellular (MagKatG1) [8] and bacterial counterparts [11]. The oxidoreductase could be purified to homogeneity and heme occupancy was almost 100%. Compared to the intracellular enzyme, MagKatG2 was less prone to proteolytic degradation during purification (Fig. 2, compare with [8]). The 3D-model as well as its ECD spectrum in the far-UV region (Supplemental Fig. 4) clearly demonstrates the Class I-typical mainly α-helical structure of MagKatG2. The bifunctional dimeric enzyme shows the typical gene-duplicated two-domain monomeric architecture, with a heme *b* containing N-terminal domain and a heme-free C-terminal domain. The active site is highly conserved and besides the proximal (His292, Trp343, Asp408) and distal amino acid triads (Arg115, Trp118, His119), found in all Class I peroxidases, it contains the unique covalent adduct Trp118-Tyr251-Met277 as shown by MS analysis (Fig. 3).

Table 1
Specific peroxidase activity of MagKatG2 probed with different electron donors at the respective pH optimum.

Type of Substrate	Electron donor	Specific activity [U/mg]	pH
One-electron donor	guaiacol	1.21 ± 0.02	6.5
	o-dianisidine	8.91 ± 0.06	6.5
	L-DOPA	7.99 ± 0.16	6.5
	resorcinol	14.21 ± 0.05	6.0
	catechol	0.95 ± 0.05	6.0
	pyrogallol	4.95 ± 0.10	5.5
	5-amino salicylic acid	7.54 ± 0.17	5.5
	ascorbate	7.32 ± 0.08	5.0
Two-electron donor	chlorination of MCD	1.75 ± 0.01	5.0
	bromination of MCD	0.035 ± 0.002	5.0
	NADH	0.91 ± 0.03	7.0

So far this posttranslational modification has been identified in X-ray structures and MS analyses of bacterial and archaeal KatGs [2,11,28–30,38] and this work for the first time describes its existence in a eukaryotic KatG. This underlines the general importance of this peculiar redox cofactor at the distal heme site for the bifunctional mechanism. Catalase–peroxidases are the only heme peroxidases that have a reasonable catalase activity, which is closely related with an intact Trp-Typ-Met adduct parallel and in close vicinity to the porphyrin ring. It was proposed that this adduct can act as radical site that enhances the turnover of oxyferrous (compound III-like) heme and avoids release of superoxide [12].

Besides these similarities regarding the overall structure and posttranslational modification KatG2 from *M. grisea* shows interesting spectral features that might reflect differences in the heme architecture compared to bacterial KatGs.

Compared to other so far investigated catalase–peroxidases, the heme spectrum is blue-shifted (Soret band at 404 nm and CT1 at 640 nm). In addition the RR core size marker bands are at high frequency, but no 6cLS heme is present. Therefore the UV–Vis and RR data suggest the presence of a QS state heme *b* reflecting a quantum mechanical admixture of intermediate- ($S = 3/2$) and high- ($S = 5/2$) spin states [39]. This is very unusual in biological systems. It has been found to be a distinctive characteristic of Class

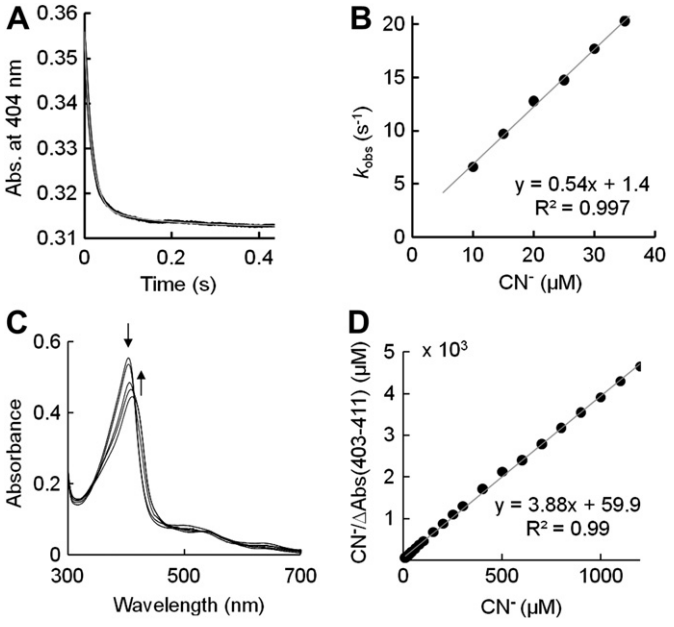

Fig. 7. Cyanide binding to MagKatG2. (A) Typical time trace at 404 nm (disappearance of high-spin MagKatG2) with single-exponential fit obtained from conventional stopped-flow spectroscopy. (B) Dependence of k_{obs} values on the cyanide concentration. The association rate constant k_{on} was calculated from the slope. (C) Spectral overlay for stepwise titration of MagKatG2 with increasing cyanide concentration. (D) Equilibrium data of titration of 5.5 μM MagKatG2 in 50 mM phosphate buffer, pH 7.0 (25 °C) with sodium cyanide presented as Hanes plot.

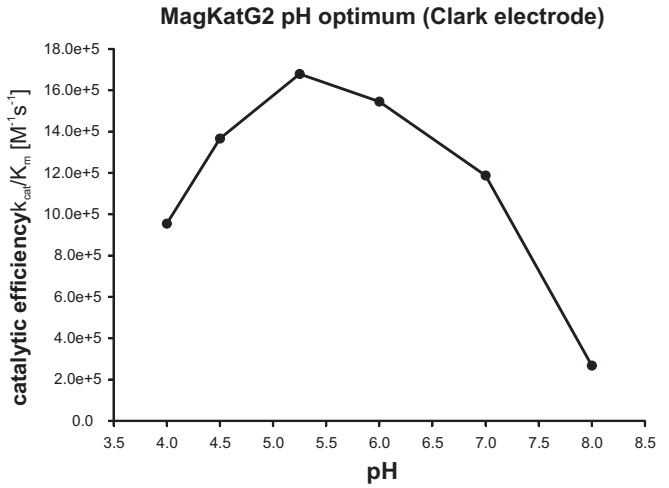

Fig. 8. pH-activity profiles for the catalytic efficiency (k_{cat}/K_m) of MagKatG2 using the Clark electrode.

III heme containing peroxidases [40,41], in which the proportion of the $S = 3/2$ state increases in the order horseradish peroxidase (HRP) < soybean peroxidases (SBP) < barley peroxidase type 1 (BP1), as suggested by the progressive increase in frequency of the core size marker bands on passing from HRP to BP1 [41].

The structural origin and functional significance of the QS states remain elusive. A saddle-shaped heme deformation appears to be a common feature of the QS hemes [42]. Interestingly, compared to other heme proteins, the low-frequency RR region of MagKatG2 is extremely rich due to a remarkable enhancement of several non-planar modes which clearly indicate the presence of a non-planar heme. In fact, RR spectroscopy applied to heme proteins has proven to be one of the best probes of the conformation of the porphyrin, due to the different activation of the structure sensitive porphyrin modes as a consequence of the planar or non-planar conformation [43]. In general, the type and magnitude of the heme plane distortion is revealed in RR spectra by the activation of non-planar modes of the heme in the 200–600 cm^{-1} region. These modes are usually Raman inactive for planar macrocycles, but become RR active in the presence of out-of-plane deformation as a consequence of the lowering of the heme group symmetry [44,45].

Further insight to the heme architecture of MagKatG2 was obtained by studying the low-frequency region RR spectrum of 5cHS of the ferrous protein which usually shows the presence of a strong band assigned to the iron–imidazole stretching mode, ν(Fe–Im), in the range 200–250 cm^{-1}. The frequency of this band is correlated to the bond strength between the iron atom and the imidazole ring and variations in the frequency of this band can be related to the imidazolate character of the proximal histidine [40,41,46]. In general, within the peroxidase–catalase superfamily, the RR spectral features of Classes I and II differ notably from those of Class III [40,41]. In fact, at neutral pH, the peroxidases belonging to the first two classes (Table 2) show a broad band due to the coexistence of two bands at very different frequencies [47–54]. They have been assigned to two tautomers: in one tautomer the proton resides on the imidazole, while in the other the proton is transferred to the carboxylate group of a nearby residue, usually an aspartate. On the contrary, peroxidases of Class III at neutral pH show only one tautomer, their RR spectra being characterized by a sharp band at relatively high frequency (Table 2). A possible explanation of this behavior might derive from a different geometry of the H-bond between the proximal His and Asp residues (of helix H) compared to the members of Classes II and III, which inhibits the formation of a double-well potential for the imidazole proton [44].

In analogy to Class I peroxidases, in the low-frequency spectrum of reduced KatG from the cyanobacterium *Synechocystis*, two ν(Fe–Im) stretching modes have been identified at 253 cm^{-1} and 205 cm^{-1} [33]. Their frequency difference is a consequence of the different strength of the hydrogen bond between the proximal His and the Asp carboxylate side chain (Supplemental Fig. 4). The band at 205 cm^{-1} corresponds to a species where the proton resides on the imidazole, whereas the band at 253 cm^{-1} corresponds to a species where the proton is almost transferred to the carboxylate group. Unlike KatG from *Synechocystis*, MagKatG2 shows only one ν(Fe–Im) stretch, whose frequency (241 cm^{-1}) is similar to that observed in KatG from *Mycobacterium tuberculosis* and to those observed for Class III peroxidases, suggesting a pronounced imidazolate character of histidine 292. Interestingly, in common with MagKatG2, the ferric form of *M. tuberculosis* KatG and Class III peroxidases is also characterized by the unusual 5cQS.

The standard reduction potential of the Fe(III)/Fe(II) couple of MagKatG2 was determined to be −210 mV, which is about 24 mV more negative than MagKatG1 [8] but within the range reported for other Class I peroxidases including *Synechocystis* KatG [21,55,56]. Only the reported value for *M. tuberculosis* KatG does not fall within this range (−58 mV, [57]).

The extracellular enzyme exhibits further differences compared to its intracellular counterpart as well as bacterial KatGs including kinetics and thermodynamics of cyanide binding and overall kinetic parameters that (together with the spectroscopic investigations) reflect some differences in the heme and substrate channel architecture. The dissociation constant K_d of MagKatG2–cyanide complex (15.4 μM) is significantly higher than in its intracellular counterpart (1.4 μM [8]) probably due to a smaller association rate. Interestingly, the pH optimum of catalase activity is in a more acidic region (pH 5.25) compared to pH 6.0 of MagKatG1, whereas the K_m, k_{cat} and k_{cat}/K_m values are similar in both branches of fungal KatGs as well as in bacterial KatGs at the respective pH optima [58]. Since in KatGs K_m significantly increases below pH optimum with decreasing pH [58] MagKatG2 is the first KatG that has a K_m value in the low millimolar region around pH 5. Recent data suggest that extracellular KatG acts primarily as catalase [9] and the observed acidic pH optimum reflects the milieu in which the extracellular fungal enzyme armory has to degrade the reactive oxygen species derived from the oxidative burst induced by the plant tissue [59]. Moreover, in the same pH region defense-related genes of the plant have been shown to be expressed [59].

As with all (prokaryotic and eukaryotic) KatGs, also for MagKatG2 the endogeneous electron donor as well as the physiological role of the peroxidatic activity is unknown. Thus, we probed various one- and two-electron donors and found reactivities that are similar in both MagKatG1 and MagKatG2 (Table 1 and [8]) except a higher chlorination and diminished bromination activity of the latter. The hierarchy of specific activities (15-fold difference) in the series resorcinol (3-hydroxyphenol) > pyrogallol (2,3-dihydroxyphenol) > guaiacol (2-methoxyphenol) > catechol (2-hydroxyphenol) suggests some specificity of binding to the yet unknown binding site. Additionally, a relatively high ascorbate oxidation rate never observed so far in a catalase–peroxidase could be measured. Although it is still about 50-times lower than that reported for ascorbate peroxidase 1 from *Pisum sativum* [60] the usage of ascorbate as electron donor for a KatG is new and the physiological role remains elusive.

Table 2
Predominant coordination and spin states observed at neutral pH and RR frequencies (cm^{-1}) of the ν(Fe–Im) stretching mode at neutral pH, for various heme containing peroxidases and selected site directed mutants of the key residues of the heme pocket. APx, ascorbate peroxidase; ScCcP, cytochrome *c* peroxidase from *Saccharomyces cerevisiae*; SynKatG, catalase–peroxidase from *Synechocystis*; MtubKatG, KatG from *Mycobacterium tuberculosis*; ARP, *Arthromyces ramosus* peroxidase; LiP, lignin peroxidase; MnP, manganese peroxidase; CIP, *Coprinus cinereus* peroxidase; HRPC and HRPA2, horseradish peroxidase isoenzyme C and A2; BP1, barley peroxidase type 1.

Protein	Fe(III) coordination and spin state	Fe(II) ν(Fe–Im) cm^{-1}	Ref.
Class I			
ScCcP	5cHS	247s 233 (sh)	[47]
ScCcP (D235N)	6cHS and 6cLS	205	[47]
APx	6cLS and 5cHS	234s 207 (w)	[48]
SynKatG	5cHS	253s 205 (w)	[33]
MtubKatG	5c (HS and QS)	244	[49]
MagKatG2	5c (HS and QS)	241	This work
Class II			
ARP/CIP	5cHS	230s 211(w)	[50]
LiP	6cHS	244s 230 (w)	[51]
MnP	6cHS	248 (s) 236 (w)	[52]
Class III			
HRPC	5c QS and 6cQS	244	[46,53]
HRPA2	5c (HS and QS)	252	[46]
SBP	5c (HS and QS)	246	[54]
BP1	5c (HS and QS)	237	[53]

Summing up, the first extracellular catalase–peroxidase was heterologously expressed. It is a typical bifunctional homodimeric mainly α-helical enzyme showing the essential posttranslational modifications that enable the enzyme to efficiently dismutate hydrogen peroxide in an acidic environment. Spectral investigations suggest a mixed-spin state and non-planar heme *b* as well as a pronounced imidazolate character of the proximal histidine and a Class I-typical standard reduction potential of its native high-spin form. Binding of cyanide is slower and weaker that in other KatGs. Various (artificial) substrates can be oxidized including ascorbate. Since secretory KatGs are only found in phytopathogenic fungi and are essential for host–pathogen interaction they are interesting targets for pest control. This, besides efficient production of recombinant native enzyme and its comprehensive biophysical/chemical characterization, needs elucidation of its X-ray structure.

Acknowledgments

This work was supported by the Austrian Science Fund FWF (to M.Z., Project P20996-B11) and ex 60% (to G.S., University of Florence). We would like to thank Prof. Lee Whitmore for consultation on DichroWeb software.

Appendix. Supplementary information

Supplementary information associated with this article can be found, in the online version, at doi:10.1016/j.biochi.2011.09.020.

References

[1] F. Passardi, N. Bakalovic, F.K. Teixeira, M. Margis-Pinheiro, C. Penel, C. Dunand, Prokaryotic origins of the non-animal peroxidase superfamily and organelle mediated transmission to eukaryotes, Genomics 89 (2007) 567–579.
[2] M. Zamocky, P.G. Furtmüller, C. Obinger, Evolution of structure and function of class I peroxidases, Arch. Biochem. Biophys. 500 (2010) 45–57.
[3] K.G. Welinder, Superfamily of plant, fungal and bacterial peroxidases, Curr. Opin. Struct. Biol. 2 (1992) 388–393.
[4] C. Obinger, Heme peroxidase biochemistry – facts and perspectives, Arch. Biochem. Biophys. 500 (2010) 1–2.
[5] M. Zamocky, C. Obinger, Molecular phylogeny of heme peroxidases. in: E. Torres, M. Ayala (Eds.), Biocatalysis Based on Heme Peroxidases. Springer, Berlin, 2010, pp. 7–35.
[6] F. Passardi, J. Favet, M. Zamocky, C. Jakopitsch, C. Penel, C. Obinger, C. Dunand, Phylogenetic distribution of catalase–peroxidases: are there patches of order in chaos? Gene 397 (2007) 101–113.
[7] M. Zamocky, P.G. Furtmüller, C. Obinger, Two distinct groups of fungal catalase/peroxidases, Biochem. Soc. Trans. 37 (2009) 772–777.
[8] M. Zamocky, P.G. Furtmüller, M. Bellei, G. Battistuzzi, J. Stadlmann, J. Vlasits, C. Obinger, Intracellular catalase/peroxidase from the phytopathogenic rice blast fungus *Magnaporthe grisea*: expression analysis and biochemical characterization of the recombinant protein, Biochem. J. 418 (2009) 443–451.
[9] S. Tanabe, N. Ishii-Minami, K.I. Saitoh, Y. Otake, H. Kaku, N. Shibuya, Y. Nishizawa, E. Minami, The role of catalase–peroxidase secreted by *Magnaporthe oryzae* during early infection of rice cells, Mol. Plant–Microbe Interact. 24 (2011) 163–171.
[10] S. Tanabe, Y. Nishizawa, E. Minami, Effects of catalase on the accumulation of H_2O_2 in rice cells inoculated with rice blas fungus, *Magnaporthe oryzae*, Physiologia Plantarum 137 (2009) 148–154.
[11] G. Smulevich, E. Droghetti, C. Jakopitsch, C. Obinger, Probing the structure and bifunctionality of catalase–peroxidase (KatG), J. Inorg. Biochem. 100 (2006) 568–585.
[12] J. Vlasits, C. Jakopitsch, M. Bernroitner, M. Zamocky, P.G. Furtmüller, C. Obinger, Mechanisms of catalase activity of heme peroxidases, Arch. Biochem. Biophys. 500 (2010) 74–81.
[13] R.A. Dean, N.J. Talbot, D.J. Ebbole, M. Farman, T. Mitchell, M. Orbach, M. Thon, R. Kulkarni, J.R. Xu, H. Pan, N.D. Read, Y.H. Lee, I. Carbone, D. Brown, Y.Y. Oh, N. Donofrio, J.S. Jeong, D.M. Soanes, S. Djonovic, E. Kolomiets, C. Rehmeyer, W. Li, M. Harding, S. Kim, M.H. Lebrun, H. Bohnert, S. Coughlan, J. Butler, S. Calvo, L.J. Ma, R. Nicol, S. Purcell, C. Nusbaum, J.E. Galagan, B.W. Birren, The genome sequence of the rice blast fungus *Magnaporthe grisea*, Nature 434 (2005) 980–986.
[14] S. Banerjee, M. Zamocky, P.G. Furtmüller, C. Obinger, Probing the two-domain structure of homodimeric prokaryotic and eukaryotic catalase–peroxidases, Biochim. Biophys. Acta 1804 (2010) 2136–2145.
[15] S. Takaichi, S. Morita, Procedures and conditions for application of the pyridine hemochrome method to photosynthetically grown cells of *Rhodopseudomonas sphaeroides*, J. Biochem. 89 (1981) 1513–1519.
[16] J.G. Lees, A.J. Miles, F. Wien, B.A. Wallace, A reference database for circular dichroism spectroscopy covering fold and secondary structure space, Bioinformatics 22 (2006) 1955–1962.
[17] L. Whitmore, B.A. Wallace, DICHROWEB, an online server for protein secondary structure analyses from circular dichroism spectroscopic data, Nucl. Acids Res. 32 (2004) W668–W673.
[18] L.J. McGuffin, K. Bryson, D.T. Jones, The PSIPRED protein structure prediction server, Bioinformatics 16 (2000) 404–405.
[19] L. Bordoli, F. Kiefer, K. Arnold, P. Benkert, J. Battey, T. Schwede, Protein structure homology modeling using SWISS-MODEL workspace, Nat. Protoc. 4 (2009) 1–13.
[20] G. Battistuzzi, M. D´Onofrio, M. Borsari, M. Sola, A.L. Macedo, J.J. Moura, P. Rodrigues, Redox thermodynamics of low-potential iron–sulfur proteins, J. Biol. Inorg. Chem. 5 (2000) 748–760.
[21] M. Bellei, C. Jakopitsch, G. Battistuzzi, M. Sola, C. Obinger, Redox thermodynamics of the ferric–ferrous couple of wild-type *Synechocystis* KatG and KatG(Y249F), Biochemistry 45 (2006) 4678–4774.
[22] D.P. Nelson, L.A. Kiesow, Enthalpy of decomposition of hydrogen peroxide by catalase at 25 degrees C (with molar extinction coefficients of H_2O_2 solutions in the UV), Anal. Biochem. 49 (1972) 474–478.
[23] A.J. Kettle, C.C. Winterbourn, Assays for the chlorination activity of myeloperoxidase, Methods Enzymol. 233 (1994) 502–512.
[24] M. Zamocky, C. Jakopitsch, J. Vlasits, C. Obinger, Fungal catalase–peroxidases – a novel group of bifunctional oxidoreductases, J. Biol. Inorg. Chem. 12 (2007) S97.
[25] S. Kim, J. Park, S.Y. Park, T.K. Mitchell, Y.H. Lee, Identification and analysis of in planta expressed genes of *Magnaporthe oryzae*, BMC Genomics 11 (2010) 104.
[26] G. Brewer, Messenger RNA decay during aging and development, Ageing Res. Rev. 1 (2002) 607–625.
[27] C. Jakopitsch, F. Rueker, G. Regelsberger, M. Dockal, G.A. Peschek, C. Obinger, Catalase–peroxidase from the cyanobacterium *Synechocystis* PCC 6803: cloning, overexpression in *Escherichia coli*, and kinetic characterization, Biol. Chem. 380 (1999) 1087–1096.
[28] R.A. Ghiladi, K.F. Medzihradszky, P.R. Ortiz de Montellano, Role of the Met-Tyr-Trp cross-link in *Mycobacterium tuberculosis* catalase–peroxidase (KatG) as revealed by KatG(M255I), Biochemistry 44 (2005) 15093–15105.
[29] C. Jakopitsch, M. Auer, A. Ivancich, F. Rueker, P.G. Furtmüller, C. Obinger, Total conversion of bifunctional catalase–peroxidase (KatG) to monofunctional peroxidase by exchange of a conserved distal side tyrosine, J. Biol. Chem. 278 (2003) 20185–20191.
[30] C. Jakopitsch, D. Kolarich, G. Petutschnig, P.G. Furtmüller, C. Obinger, Distal side tryptophan, tyrosine and methionine in catalase–peroxidases are covalently linked in solution, FEBS Lett. 552 (2003) 135–140.
[31] S. Choi, T.G. Spiro, K.G. Langry, K.M. Smith, D.L. Budd, G.N. LaMar, Structural correlations and vinyl influences in resonance Raman spectra of protoheme complexes and proteins, J. Am. Chem. Soc. 104 (1982) 4345–4351.
[32] M.P. Marzocchi, G. Smulevich, Relationship between heme vinyl conformation and the protein matrix in peroxidases, J. Raman Spectros. 34 (2003) 725–736.
[33] H.A. Heering, C. Indiani, G. Regelsberger, C. Jakopitsch, C. Obinger, G. Smulevich, New insights into the heme cavity structure of catalase–peroxidase: a spectroscopic approach to the recombinant synechocystis enzyme and selected distal cavity mutants, Biochemistry 41 (2002) 9237–9247.
[34] Q. Huang, R. Schweitzer-Stenner, Non-planar heme deformations and excited state displacements in horseradish peroxidase detected by Raman spectroscopy at Soret excitation, J. Raman Spectros. 36 (2005) 363–375.
[35] S. Hu, K.M. Smith, T.G. Spiro, Assignment of protoheme resonance Raman spectrum by heme labeling in myoglobin, J. Am. Chem. Soc. 118 (1996) 12638–12646.
[36] S. Hu, I.K. Morris, J.P. Singh, K.M. Smith, T.G. Spiro, Complete assignment of cytochrome c resonance Raman spectra via enzymatic reconstitution with isotopically labeled hemes, J. Am. Chem. Soc. 115 (1993) 12446–12458.
[37] T.G. Spiro, X.-Y. Li, in: T.G. Spiro (Ed.), Resonance Raman Spectroscopy of Metalloporphyrins, John Wiley & Sons, New York, 1988.
[38] X. Carpena, S. Loprasert, S. Mongkolsuk, J. Switala, P.C. Loewen, I. Fita, Catalase–peroxidase KatG of *Burkholderia pseudomallei* at 1.7 A° resolution, J. Mol. Biol. 327 (2003) 475–489.
[39] C. Indiani, A. Feis, B.D. Howes, M.P. Marzocchi, G. Smulevich, Benzohydroxamic acid–peroxidase complexes: spectroscopic characterization of a novel heme spin species, J. Am. Chem. Soc. 122 (2000) 7368–7376.
[40] G. Smulevich, A. Feis, B.D. Howes, Fifteen years of Raman spectroscopy of engineered heme containing peroxidases: what have we learned? Acc. Chem. Res. 38 (2005) 433–440.
[41] G. Smulevich, A. Feis, B.D. Howes, A. Ivancich, Structure–function relationships among heme peroxidases: new insights from electronic absorption, resonance Raman and multifrequence electron paramagnetic resonance spectroscopies. in: K.M. Kadish, K.M. Smith, R. Guilard (Eds.), Handbook of Porphyrin Science. World Scientific, Singapore, 2010, pp. 367–453.
[42] R.J. Cheng, P.Y. Chen, P.R. Gau, C.C. Chen, S.M. Peng, Control of spin state by ring conformation of Iron (III) porphyrins. A novel model for the quantum-mixed intermediate spin state of ferric cytochrome c′ from photosynthetic bacteria, J. Am. Chem. Soc. 119 (1997) 2563–2569.

[43] J.A. Shelnutt, X.-Z. Song, J.-G. Ma, S.-L. Jia, W. Jentzen, C.J. Medforth, Nonplanar porphyrins and their significance in proteins, Chem. Soc. Rev. 27 (1998) 31–41.
[44] M.E. Blackwood Jr., T.S. Rush III, F. Romesberg, P.G. Schultz, T.G. Spiro, Alternative modes of substrate distortion in enzyme and antibody catalyzed ferrochelation reactions, Biochemistry 37 (1998) 779–782.
[45] S. Choi, T.G. Spiro, Out-of-plane deformation modes in the resonance Raman spectra of metalloporphyrins and heme proteins, J. Am. Chem. Soc. 105 (1983) 3683–3692.
[46] J. Teraoka, T. Kitagawa, Structural implication of the heme-linked ionization of horseradish peroxidase probed by the Fe–histidine stretching Raman line, J. Biol. Chem. 256 (1981) 3969–3977.
[47] G. Smulevich, J.M. Mauro, L.A. Fishel, A.M. English, J. Kraut, T.G. Spiro, Heme pocket interactions in cytochrome c peroxidase studied by site-directed mutagenesis and resonance Raman spectroscopy, Biochemistry 27 (1988) 5477–5485.
[48] M. Nissum, F. Neri, D. Mandelman, T.L. Poulos, G. Smulevich, Spectroscopic characterization of recombinant pea cytosolic ascorbate peroxidase: similarities and differences with cytochrome *c* peroxidase, Biochemistry 37 (1998) 8080–8087.
[49] K. Ranguelova, J. Suarez, L. Metlitsky, S. Yu, S.Z. Brejt, S.Z. Brejt, L. Zhao, J.P. Schelvis, R.S. Magliozzo, Impact of distal side water and residue 315 on ligand binding to ferric *Mycobacterium tuberculosis* catalase–peroxidase (KatG), Biochemistry 47 (2008) 12583–12592.
[50] G. Smulevich, A. Feis, C. Focardi, J. Tams, K.G. Welinder, Resonance Raman study of the active site of *Coprinus cinereus* peroxidase, Biochemistry 33 (1994) 15425–15432.
[51] D. Kuila, M. Tien, J.A. Fee, M.R. Ondrias, Resonance Raman spectra of extracellular ligninase: evidence for a heme active site similar to those of peroxidases, Biochemistry 24 (1985) 3394–3397.
[52] Y. Mino, H. Wariishi, N.J. Blackburn, T.M. Loehr, M.H. Gold, Spectral characterization of manganese peroxidase, an extracellular heme enzyme from the lignin-degrading basidiomycete, *Phanerochaete chrysosporium*, J. Biol. Chem. 263 (1988) 7029–7036.
[53] B.D. Howes, C.B. Schiødt, K.G. Welinder, M.P. Marzocchi, J.-G. Ma, J. Zhang, J.A. Shelnutt, G. Smulevich, The quantum mixed-spin heme state of barley peroxidase: a paradigm for class III peroxidases, Biophysical J. 77 (1999) 478–492.
[54] M. Nissum, A. Feis, G. Smulevich, Characterization of soybean seed coat peroxidase: resonance Raman evidence for a structure based classification of plant peroxidases, Biospectroscopy 4 (1998) 355–364.
[55] G. Battistuzzi, M. Bellei, C.A. Bortolotti, M. Sola, Redox properties of heme peroxidases, Arch. Biochem. Biophys. 500 (2010) 21–36.
[56] J. Vlasits, M. Bellei, C. Jakopitsch, F. De Rienzo, P.G. Furtmüller, M. Zamocky, M. Sola, G. Battistuzzi, C. Obinger, Disruption of the H-bond network in the main access channel of catalase–peroxidase modulates enthalpy and entropy of Fe(III) reduction, J. Inorg. Biochem. 104 (2010) 648–656.
[57] N.L. Wengenack, H. Lopes, M.J. Kennedy, P. Tavares, A.S. Pereira, I. Moura, J.J.G. Moura, F. Rusnak, Redox potential measurements of the *Mycobacterium tuberculosis* heme protein KatG and the isoniazid-resistant enzyme KatG(S315T): insights into isoniazid activation, Biochemistry 39 (2000) 11508–11513.
[58] R. Singh, B. Wiseman, T. Deemagarn, V. Jha, J. Switala, P.C. Loewen, Comparative study of catalase–peroxidases (KatGs), Arch. Biochem. Biophys. 471 (2008) 207–214.
[59] S. Tanabe, N. Hayashi, Y. Nishizawa, H. Yamane, N. Shibuya, E. Minami, Elicitor and catalase activity of conidia suspensions of various strains of *Magnaporthe grisea* in suspension-cultured cells of rice, Biosci. Biotechnol. Biochem. 72 (2008) 889–892.
[60] R. Mittler, B.A. Zilinskas, Purification and characterization of pea cytosolic ascorbate peroxidase, Plant Physiol. 97 (1991) 962–968.